In situ hydromechanical responses during well drilling recorded by distributed fiber-optic strain sensing

Yi Zhang[1,2], Xinglin Lei[3], Tsutomu Hashimoto[1,2], Ziqiu Xue[1,2]

5 [1] Geological Carbon Dioxide Storage Technology Research Association, Kyoto, 6190292 Japan.
   [2] Research Institute of Innovative Technology for the Earth (RITE), Kyoto, 619-0292 Japan.

   [3] Geological Survey of Japan, National Institute of Advanced Industrial Science and Technology, Tsukuba, 305-8567, Japan.

Correspondence to: Yi Zhang (zhangyi@rite.or.jp)

10 **Abstract.** Drilling fluid infiltration during well drilling induces pore pressure and strain perturbations in neighboured reservoir formations. In this study, we in situ monitored such small strain changes (~ 20 µε) using fiber-optic distributed strain sensing in two observation wells with different distances (approximately 3 m and 9 m) from a new drilling wellbore in a shallow water aquifer. The results suggest that the drilling induced hydromechanical deformations that occurred at depths of both wells are indicative of the impact zones of fluid invasion and reservoir permeability structure (heterogeneity). A hydraulic diffusion
15 model is used to interpret the strain evolution. The method and data would be useful for understanding reservoir pressure communications, determining the zones for fluid productions or injections (e.g., for CO_2 storage), and optimizing reservoir management and utilization.

1 Introduction

20 The utilization of underground reservoirs includes exploitation or storage of resources such as groundwater, oil/gas, heat, and more recently, the CO_2 for mitigating the effect of CO_2 emission on global warming (Benson et al., 2005), as well as storage of compressed air for electric energy storage (Mouli-Castillo et al., 2019) in underground reservoirs. For better utilization, an understanding of fluid flow and reservoir characteristics is required for more manageable and optimized operations. Geophysical methods, such as site-scale seismic, electrical methods, and well logging, have been widely applied for reservoir
25 characterization and monitoring.

Distributed fiber optic sensing is emerging as a novel and practical technology for underground reservoir monitoring by measuring environmental changes of physical fields, such as temperature, strain and elastic waves (Barrias et al., 2016; Schenato, 2017; Shanafield et al., 2018). There have been numerous application studies using distributed temperature sensing (DTS) and distributed acoustic sensing (DAS) in subsurface monitoring. DTS data have been useful for understanding fluid

30   flow behaviour (such as flow rate and active fluid flow zone) and reservoir characteristics owing the hydro-thermal coupling in addition to heat transport monitoring (Bense et al., 2016; Freifeld et al., 2008; Luo et al., 2020; Maldaner et al., 2019; des Tombe et al., 2019). DAS has been intensively developed and used to monitor surface, subsurface shallow reservoirs or deep structures (Daley et al., 2013; Jousset et al., 2018; Lellouch et al., 2019; Lindsey et al., 2019, 2020; Zhu and Stensrud, 2019). On the other hand, the usage of distributed strain sensing (DSS) for subsurface monitoring is comparatively less.

35   Although the main purpose of DSS is the monitoring of geomechanical deformations or earth subsidence (for safety considerations) (Kogure and Okuda, 2018; Murdoch et al., 2020; Zhang et al., 2018), DSS could also be used to understand reservoir formation and reservoir flow owing to hydro-mechanical coupling. In principle, the physical coupling between fluid flow and strain is understood by the linear poroelasticity theory (Biot, 1941). In poroelastic theory, the deformation, such as soil consolidation, can induce "solid-to-fluid" coupled pressure change and fluid flow, whereas conversely, the fluid flow with

40   pressure change can modify the effective stress of reservoir formation and cause "fluid-to-solid" coupled deformations (Cheng, 2016; Neuzil, 2003; Wang, 2017). The deformations could be the expression of fluid flow behaviour in the reservoir and bear information regarding fluid flow and reservoir characteristics (such as permeability and compressibility) (Barbour and Wyatt, 2014; Schuite et al., 2015, 2017; Schweisinger et al., 2009; Zhang and Xue, 2019). By monitoring strain changes of an aquifer, fluid-to-solid coupling can characterize the hydraulic parameters in the reservoir formation.

45   Deformation-based reservoir monitoring methods have been recently applied to obtain the lateral permeability distribution (at coarse-scales) of underground reservoirs with surface deformations monitored by InSAR technique (Bohloli et al., 2018; Vasco et al., 2008, 2010) and estimate vertical compressibility with vertical deformation measured by well-based techniques (e.g., radioactive maker technique and extensometer stations) (Ferronato et al., 2003; Hisz et al., 2013; Murdoch et al., 2015). However, such vertical deformation monitoring tools are usually only available at limited points and over limited time intervals.

50   In addition, it is not well understand the contribution of each formation zone to the total surface displacement.

It could be suitable for in situ monitoring of such hydromechanical responses in reservoirs via the high accuracy and resolution of DSS using optical fibers. Several studies have used the DSS tool to demonstrate that the deformation records during fluid injection in rocks can be utilized to obtain information of permeability, compressibility, and track pressure and fluid plume migration in laboratory experiments (Xue et al., 2018; Zhang et al., 2019; Zhang and Xue, 2019). Becker et al. (2017), Lei et

55   al. (2019) and Sun et al. (2020) have recent shown that the hydromechanical responses during reservoir testing (water injection or extraction) can be effectively monitored via DSS. These studies suggest the high application potential of the DSS tool in field studies for monitoring underground fluid reservoirs.

In addition to purposed reservoir testing, the well drilling process itself also develops hydromechnical processes—drilling fluid (also called mud) can infiltrate reservoir formation under the high pressure drive from the wellbore and deform the

60   formation. Though the phenomenon and its role in reservoir damage have been well studied, its role in reservoir characterization has generally been overlooked. Considering the hydromechanical response, the spatial variations in reservoir permeability heterogeneity are expected to affect the pattern of formation deformation. Conversely, the deformation pattern could be indicative of the formation permeability structure.

In order to demonstrate this idea, we examine the DSS records of a field study with strain monitoring in two wells (optical

65 fiber installed) using DSS while drilling a new well. The results suggest that the high-resolution DSS data acquired during well drilling could be used to understand reservoir lithological changes and permeability structure. In this paper, we first introduce the measurement principle of high-resolution DSS based on Rayleigh scattering, field site operations with considering the installation method, then present the results of monitoring using DSS while well drilling, and finally provide the estimation of permeability using a pressure diffusion model. Some implications and potential applications are emphasized.

70 **2 Methods**

Optical fiber sensors work with the concept that the environmental effects, e.g., strain, temperature, can alter the phase, frequency, spectral content, and power of backscattered lights propagated through an optical fiber. There are three types of scattering mechanisms—Raman, Brillouin, and Rayleigh scattering—used for measuring temperature or strain changes. In this study, we only consider the Rayleigh backscattering based method.

75 Rayleigh backscattering occurs when light propagates due to the existence of small random optical defects or impurities in the fiber core. Rayleigh backscatter spectrum of a point in an optical fiber can be considered as a fingerprint of the fiber. In conventional coherent optical time-domain reflectometer (COTDR) method, Rayleigh backscatter spectrum of generated for each region in the longitudinal direction of the optical fiber is obtained through measurement (Fig. S1) (Hartog, 2017). From frequency shift between the reference Rayleigh-scattering power spectrum (RSPS) and a target RSPS using the cross-

80 correlation method, strain or temperature change at the point can be calculated. The distance of the scattering occurrence to the input end can be calculated using the travel time of scattered light. Because the length of light pulse in COTDR is large, the spatial resolution of conventional COTDR is low.

In order to obtain high spatial resolution, the pulse lengths of incident light must be shortened. However, if the pulse is shortened, the light pulse energy and thus the signal intensity of the backscatters are lowered and the measurement accuracy

85 becomes low at positions distant from the input end. For overcoming the limitations of conventional COTDRs, in the new tuneable-wavelength coherent optical time-domain reflectometer (TW-COTDR) method, the tuneable wavelength distributed feedback laser and chirp signals by frequency sweeping and modulation methods are used to shorten laser light pulses while simultaneously ensuring sufficient pulse intensity (Kishida et al., 2014; Koyamada et al., 2009). To enhance the intensity of chirped signals and suppress the range side lobe, Gaussian amplitude modulation is performed. An inverse chirp filter is used

90 to obtain RSPS in the analysis. Finally, the cross correlation method is used for calculating the frequency shift amount of the spectrum, which is further used to calculate the strain or temperature change. TW-COTDR offers the ability of single-end accessing distributed measurements, high sensitivity, wide range of spatial resolutions, and measurements over long distances. Each distributed point (a short portion) along the entire length of an optical fiber can be taken as a sensing element.

The frequency shift (Δf) caused by strain and temperature changes ($\Delta \epsilon$ and ΔT) can be linearly described using the following

95 simple equation,

$$\Delta f = A\Delta\epsilon + B\Delta T \tag{1}$$

where A and B (are the coefficients) relate the frequency shift to strain and temperature changes. Under the condition of constant temperature ($\Delta T = 0$, assumed in this study), the frequency shift (Δf) simply becomes proportional to the strain changes ($\Delta\epsilon$) by A. A is -0.140 GHz/$\mu\epsilon$ for the optical fiber used in this study. The value was obtained from a prior calibration

100   measurement, which was conducted using the tensile tester with a displacement gauge. We used an optical interrogator NBX-SR7000 (Neubrex Co., Ltd., Japan) with TW-COTDR function in this study (Kishida et al., 2014). The instruments can provide high measurement accuracy (0.5 $\mu\epsilon$) and spatial resolution (5 cm), allowing for the monitoring of very small strains over long-distances (~25 km) in a distributed manner.

3 Field study

105   The field test site is located in the rural area of Mobara city (Chiba, Japan). There are two preexisting vertical wells (obs1 and obs2) with prior installations of optical fiber cables, by installing optical fiber cables behind the casing of the wellbores. In engineering practice, because the silica-fabricated nude optical fiber itself is thin and weak, the fabricated fiber cable using extrinsic reinforced jackets are necessary for protecting the central fiber core and practically installing the fiber in underground wellbores. A stainless steel wire reinforced cable (strain cable) was deployed. In the fiber cable, two stainless steel wires

110   (SUS304 WBP) are assembled alongside the fiber core (SR15) in the polyolefin elastomer body (Fig. S2). During the installation, the cable with each segment of steel casing was carefully placed downward to the wellbore. The cable was fixed using specially designed clamps, placing the fiber cable between the casing and the formation (Fig. 1c).

Cementing operations with injection of cement slurry were undertaken to further fix the fiber cable and seal the annulus after the siting of the casing. The cementing operations must be conducted with sufficient care to ensure the integrity of the entire

115   cementing string and avoid sudden downward migration of the cement column or development of new local cracks or sudden compressions, which, in combination with large local strains, may damage the fiber. The cable's width and height are approximately 3.8 and 2.0 mm, respectively. Another kind of fiber cable (temperature cable) with solely sensitivity to temperature was also installed for examining the in situ temperature changes. After well completion with fiber cable installation, the wellbore and formations were equilibrated for a long duration of time (e.g., a month) to reach stability before further

120   monitoring of reservoir testing. The data obtained during this period can be used to evaluate the cementing job and the well stability.

In this study, a new well was drilled approximately 3 m from one observation well and 9 m from the other (Fig. 1a). The diameter of the new well was approximately 15.9 cm. The final drilling depth was 186.5 m. During the drilling, a NP-700 mud pump was used to pump out and circulate the drilling fluid (mud water) flowing in the well; this was done to remove cuttings

125   and maintain wellbore stability. The bentonite clay-based and Ribonite adjusting agents were intermittently and manually added to the drilling fluid. The drilling fluid had a density approximately 1.1 kg/L and a high viscosity (the value is unknown), which require a high pressure to drive the drilling fluid to circulate in the well.

Solid Earth
Discussions
Open Access
EGU

The drilling fluid can partially invade the reservoir formation or permeable layers in the lateral direction under the high pressure conditions at the wellbore (Fig. 1b). This produced hydromechanical deformations in the areas where the pressure propagating

130   towards. It is common that a reservoir develops layered heterogeneities such as the sandstone-mud alternations in this study. Correspondingly, there are vertical changes in permeability in such lithological layers or zones. The changes are expected to guide the pattern of fluid infiltration, pressure change, and formation deformation. Conversely, the pattern of deformation could be indicative of permeability structure and fluid flow.

We monitored the real-time strain changes at obs1 and obs2 using DSS while drilling the new well. The fiber optic acquisition

135   was performed using the Neubrescope NBX-SR7000 device in quick measurement mode (approximately 2 min/record). The optical fibers for the two wells were connected to the acquisition device through separate channels. We used an optical switch to routinely distribute measurement jobs to each channel. One of the purposes of this study was to test the performance of these DSS tools with the designed cables and wellbore-based installations.

4 Results and implications

140   DSS records obtained during the drilling of the new well were graphed as time-depth-strain value contour images, depth-strain value profiles, and strain value-time curves (Fig. 2-3 and S3). In these figures, the time-lapse changes in strain responses accompanying the drilling process are clearly revealed at the locations of both the obs1 and obs2 wells. The spatiotemporal changes in strain are indicative of each drilling interval. Figure 1a and b show that the onset of positive strain change (expansion) corresponds to the start of drilling process at each depth (Fig. 2-3). Strain records clearly indicate the downward

145   migration of drilling operation. Phase delays appear at both wells for strain records at depths of approximately 71, 87, and 144 m (Fig. S3a and b). The drilling process left a marked trace in the images.

Moreover, the spatiotemporal patterns of changes in strain in the two observation wells match the layered aquifer structure. The different magnitudes of the changes of strain in the two wells—smaller changes developed in obs2 than in obs1—may indicate the diffusion of radial pressure and attenuation from near to far field (Fig. 1a and b) along strata. The drilling fluid

150   invasion induced fluid pressure propagated mostly along the layers. The greatest expansion strain that developed at the closer obs1 well is approximately 25 $\mu\epsilon$ (which is still a small value) whereas at the obs2 well it is approximately 10 $\mu\epsilon$ (Fig. 3f). Furthermore, variations in strain magnitude in the vertical direction appear at different depths, indicating depth-dependent lithological heterogeneities (sandstone-mudstone alternations) and permeability changes. These strain peaks may indicate more permeable layers. Fig. S3 shows the well logs of compressive and shear wave velocities (Vp and Vs) in the depth range between

155   100 m and 150 m. The lithological changes can be also visible from Vp and Vs logs. Compared to the Vp and Vs, the distributed strain records show a more clear pattern of formation structure. In addition, there appears to be a trend in which strain magnitude increases with respect to depth. This may be related to the increased pressure at the wall of the drilling well to greater depths, which is caused by the increasing density of drilling fluid under the effect of gravity.

Among these positive strain peaks, the transition layers show negative (compressive) strains. The compressive deformations

160   may be caused by the mechanical compensation effect in which adjacent upper and lower layers with low permeability are passively compressed by expansion layers. The dilation deformation was generally larger than the compressive deformation (Fig. 3f). Overall, the entire formation should show a dilation deformation, which may result a weak uplift on the surface. Previously, the surface displacement caused by fluid injection or extraction has been investigated using geodetic techniques (e.g., InSAR) and used to estimate reservoir properties (Bohloli et al., 2018; Grapenthin et al., 2019; Jiang et al., 2018; Smith

165   and Knight, 2019; Vasco et al., 2010, 2017). Here our results suggest the dilation deformation caused by drilling fluid injection may be partially compensated by adjacent zones. Therefore, using solely surface data to estimate reservoir hydraulic parameters may need to consider the compensation effect. Vertical well based DSS and surface based monitoring methods complement each other in resolution and dimension.

In Fig. S4a and b, the variations in the strain values with respect to time may reflect the time-dependent pressure propagation

170   during drilling. At the initial stage after drilling reached the depths, there were some diffusion-controlled changes as the strain increased gradually; however, after the strain developed some values, there were some irregular variations followed by a gradual reduction in strain values. The irregular variations and reduction might be due to the instabilities of drilling operations and the redistributing of total flux with the ongoing drilling to new depths. The unstable addition of drilling fluid at the surface could also be for the changes. Regardless, most of the raw strain data (time-series) show a quite good trend, manifesting high

175   quality data and a good DSS performance. The subtle hydromechanical deformations caused by well drilling have been captured clearly. Besides, the changes were not relevant to temperature. The records of another optical fiber sensing cable with solely sensitivity to temperature (and insensitive to strain) show no apparent change in temperature at the locations of obs1 and obs2.

The difference in strain changes at obs1 and obs2 could be reasonably understood by considering a pressure diffusion model.

180   There was a pressure change (ΔP_0) at the drilling location due to the circulation of drilling fluid relative to the hydrostatic formation pressure. The radial pressure diffusion caused further pressure changes (ΔP_1 and ΔP_2) at the depths of wells obs1 and obs2, as controlled by the permeability of the layer (Fig. S5). Consequently, corresponding changes occurred for effective stress (σ_1 and σ_2) and strain (ε_1 and ε_2) at these sites. Therefore, we can estimate pressure changes (ΔP_1 and ΔP_2) using the measured strain values (ε_1 and ε_2) with possible elastic constants.

185   Here we use the generalized radial flow model (Barker, 1988) to interpret the above description of pressure diffusion. We give rough estimations by considering only the pressure change due to the static density increment ($\Delta\rho$, approximately 100 kg/m3) of drilling fluid. The pressure change at the drilling well can be estimated as $\Delta P_0 = \Delta\rho gh$, where g is the gravity constant and h is the depth. The pressure of each depth can be viewed as a constant pressure head in the model. The analytical form of Barker's solution for pressure change $\Delta P(r,t)$ at distance r, time t is given as follows:

190    $$\Delta P(r,t) = \frac{\mu Q r^{2-n}}{4k\pi^{0.5n}}\Gamma(\frac{n}{2}-1,\frac{S_s r^2 \mu}{4k\rho gt}) \tag{2}$$

where μ is the water viscosity (6.7×10^{-10} Pa·S), Q is the flow rate, $n = 2$ is the problem dimension, k is the permeability, ρ is the density (1000 kg/m³), g is the gravity constant (9.8 m/s²), and Γ denotes the complementary incomplete gamma function. The specific storage S_s can be related to vertical formation compressibility c as $S_s = \rho g(c + \varphi\beta)$, where φ is the porosity (0.1) and β is the water compressibility (6.7×10^{-10} 1/Pa).

195 Therefore, in the generalized radial flow model, both the effects of hydraulic conductivity and specific storage (or permeability and compressibility) are considered. This can be viewed as a simplified poroelastic equation(s) considering only the elastic effect along the vertical direction (uniaxial deformation). Besides, the Theis or Jacob and Lohman solutions can be viewed as a simplified version of the above model. Here we use Barker's model for its generality.

The vertical strain ε can be linearly related to the pore pressure change ΔP through vertical compressibility c. However, we
200 apply a constant c (5×10^{-10} 1/Pa or specific storage 5.5×10^{-6}) for all layers. Using a least squares algorithm, we search the model parameters that best matched the measured strains at obs1 and obs2. In the estimation, there two free parameters: permeability and flow rate. We only use the data from the initial diffusion stage of the drilling at a depth interval.

Fig. 4a-f show the best-matched model of pressure diffusion at the sites of wells obs1 and obs2 for each selected layer (1–6). The modelling results suggest the detected strain changes are explainable by drilling induced pressure diffusion. In addition,
205 Fig. 4a-f show that the strain induced by the small pressure changes (e.g., above approximately 1 kPa) in the reservoir can be captured by the DSS. This is consistent with our laboratory testing results (Zhang and Xue, 2019). It suggests that DSS can be used to monitor reservoir pressure in the remote regions with small degree of changes and probably fit the purpose of hydraulic tomography (Yeh and Liu, 2000). The distributed and continuous monitoring of DSS for pressure responses would provide greater convenience in the application of hydraulic tomography than conventional discrete sensors.

210 Table 1 outlines the used permeability values in the modelling for each layer at wells obs1 and obs2. The permeability estimated using the strain values at obs1 well shows larger variations, ranging between 7.0×10^{-17}–2.7×10^{-15} m²; whereas that estimated at obs2 well shows smaller variations ranging between 3.6×10^{-16}–7.7×10^{-16} m². The inconsistency is probably due to the invasion of drilling fluid affecting the permeability of regions near the drilling location more than it affects others. Table S1 lists the fitted flow rate in the modelling. The flow rate ranges between 2.0×10^{-7}–2.8×10^{-6} m³/s.

215 Note that the parameters are still with large uncertainties as the complicated field operations and the simplicity of the model. Nevertheless, our modelling suggests that the DSS records can be explained by the hydromechanical responses of pressure diffusion and that the strain pattern is indicative of the permeability structure.

5 Conclusions

Pore fluid extractions from or injections into reservoirs can induce changes in fluid pressure, modify effective stress, and
220 deform aquifer formation. Before massive changes in mass, such fluid-to-solid hydromechanical (HM) deformations are usually subtle, linearly elastic, and recoverable; however, the deformations are often neglected because the stratum formation remains stable. In this study, we successfully measured such weak HM deformations induced by small pressure perturbations

(e.g., 1 kPa) using a high-resolution DSS tool during well drilling. Both observation wells recorded the clear strain changes that accompanied well drilling operations. The good correlation of the pattern of deformation between the two wells perhaps

225   indicates the vertical lithological heterogeneity of the formation.

Here DSS provides more details of reservoir deformation along the vertical direction, which should be helpful for understanding the contribution of each layer to the overall displacement. One worthy noting issue is that the dilation deformation caused by drilling fluid injection may be compensated by adjacent layers or zones. Therefore, one may need to be cautious for the compensation effect when using solely surface geodetic data to estimate reservoir hydraulic parameters.

230   Vertical observation through DSS and surface based monitoring methods (e.g., InSAR) complement each other in resolution and dimension.

We interpret the strain evolution by matching the pressure responses to a theoretical pressure diffusion model (Barker, 1988). Though the modelling is limited by the assumption of compressibility and some uncertainties (e.g., the skin effect due to mud cake), it suggests that the DSS records made during well drilling can be reasonably explained by the hydromechanical

235   responses of pressure diffusion and that the strain pattern is indicative of the permeability structure. An improved estimation could be performed using data acquired at a stage with a more stable diffusion process, for example during the pressure or strain recovery stages after drilling.

This study demonstrated the good performance of a Rayleigh scattering-based DSS using TW-COTDR method. Beyond the usage of DSS for monitoring aquifer deformation, a functionality similar to the one shown in this study could be deployed to

240   tracking fluid behaviour and characterize underground fluid storage reservoirs (e.g., those for natural fluids such as water, gas and oil, or those used for geological storage of CO_2) (Murdoch et al., 2020; Vilarrasa et al., 2013). Because the high resolution and accuracy, the use of DSS would be beneficial in operations involving hydromechanical responses; for reservoir testing and proper fluid injection or extraction; pressure management; the detection of fluid leakage from reservoirs (Rutqvist et al., 2016) or pipelines buried in sediment; rock fracking and stimulation (Krietsch et al., 2020), and optimizing reservoir utilization.

245   DSS could be also deployed in studying natural processes involving hydromechanical responses, such as at seismogenic structures (e.g., faults) related to earthquake occurrences (Kinoshita and Saffer, 2018)(Guglielmi et al., 2020).

Data availability. The strain data are available at 10.6084/m9.figshare.12009504.

250   Author contributions. YZ performed the analysis and processed the data. TH contributed to the acquisition of field data. ZX managed the project. YZ drafted the manuscript. All authors discussed the results and contributed to the final article.

Competing interests. The authors declare that they have no conflict of interest.

Solid Earth
Discussions

Open Access

EGU

References

Barbour, A. J. and Wyatt, F. K.: Modeling strain and pore pressure associated with fluid extraction: The Pathfinder Ranch
260   experiment, J. Geophys. Res. Solid Earth, 119(6), 5254–5273, doi:10.1002/2014JB011169, 2014.

Barker, J. A.: A generalized radial flow model for hydraulic tests in fractured rock, Water Resour. Res., 24(10), 1796–1804,
1988.

Barrias, A., Casas, J. and Villalba, S.: A review of distributed optical fiber sensors for civil engineering applications,
Sensors, 16(5), 748, 2016.

265   Becker, M. W., Ciervo, C., Cole, M., Coleman, T. and Mondanos, M.: Fracture hydromechanical response measured by fiber
optic distributed acoustic sensing at milliHertz frequencies, Geophys. Res. Lett., 44(14), 7295–7302, 2017.

Bense, V. F., Read, T., Bour, O., Le Borgne, T., Coleman, T., Krause, S., Chalari, A., Mondanos, M., Ciocca, F. and Selker,
J. S.: Distributed T emperature S ensing as a downhole tool in hydrogeology, Water Resour. Res., 52(12), 9259–9273, 2016.

Benson, S., Cook, P., Anderson, J., Bachu, S., Nimir, H. B., Basu, B., Bradshaw, J., Deguchi, G., Gale, J. and von Goerne,
270   G.: Underground geological storage, IPCC Spec. Rep. carbon dioxide capture storage, 195–276, 2005.

Biot, M. A.: General theory of three-dimensional consolidation, J. Appl. Phys., 12(2), 155–164, 1941.

Bohloli, B., Bjørnarå, T. I., Park, J. and Rucci, A.: Can we use surface uplift data for reservoir performance monitoring? A
case study from In Salah, Algeria, Int. J. Greenh. Gas Control, 76, 200–207, 2018.

Cheng, A. H.-D.: Poroelasticity., 2016.

275   Daley, T. M., Freifeld, B. M., Ajo-Franklin, J., Dou, S., Pevzner, R., Shulakova, V., Kashikar, S., Miller, D. E., Goetz, J. and
Henninges, J.: Field testing of fiber-optic distributed acoustic sensing (DAS) for subsurface seismic monitoring, Lead. Edge,
32(6), 699–706, 2013.

Ferronato, M., Gambolati, G., Teatini, P. and Baù, D.: Interpretation of radioactive marker measurements to evaluate
compaction in the Northern Adriatic gas fields, SPE Reserv. Eval. Eng., 6(06), 401–411, 2003.

280   Freifeld, B. M., Finsterle, S., Onstott, T. C., Toole, P. and Pratt, L. M.: Ground surface temperature reconstructions: Using in
situ estimates for thermal conductivity acquired with a fiber-optic distributed thermal perturbation sensor, Geophys. Res.
Lett., 35(14), doi:10.1029/2008GL034762, 2008.

Grapenthin, R., Kelley, S., Person, M. and Folsom, M.: Decadal-Scale Aquifer Dynamics and Structural Complexities at a
Municipal Wellfield Revealed by 25 Years of InSAR and Recent Groundwater Temperature Observations, Water Resour.
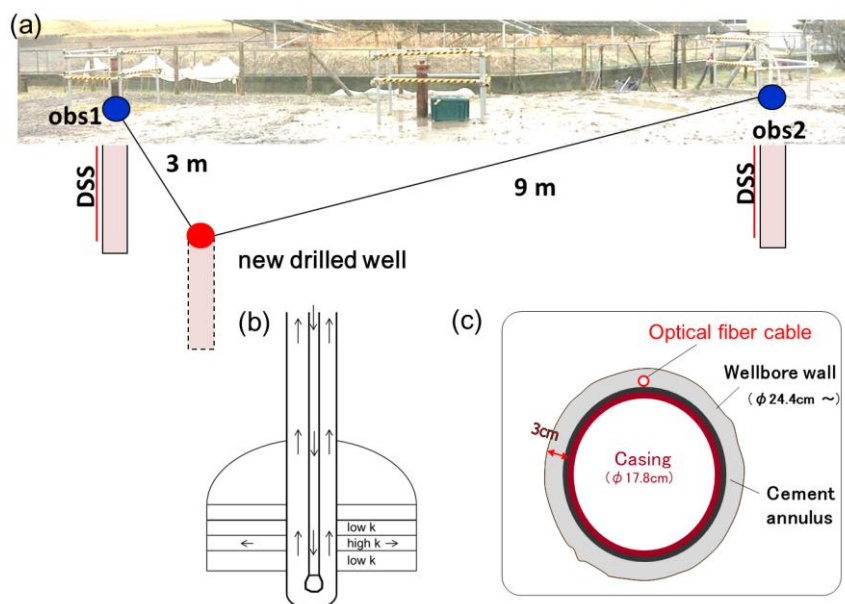285   Res., 55(12), 10636–10656, doi:10.1029/2018WR022552, 2019.

Guglielmi, Y., Nussbaum, C., Jeanne, P., Rutqvist, J., Cappa, F. and Birkholzer, J.: Complexity of Fault Rupture and Fluid Leakage in Shale: Insights From a Controlled Fault Activation Experiment, J. Geophys. Res. Solid Earth, 125(2), e2019JB017781, doi:10.1029/2019JB017781, 2020.

Hartog, A. H.: An introduction to distributed optical fibre sensors, CRC press., 2017.

290 Hisz, D. B., Murdoch, L. C. and Germanovich, L. N.: A portable borehole extensometer and tiltmeter for characterizing aquifers, Water Resour. Res., 49(12), 7900–7910, doi:10.1002/wrcr.20500, 2013.

Jiang, L., Bai, L., Zhao, Y., Cao, G., Wang, H. and Sun, Q.: Combining InSAR and Hydraulic Head Measurements to Estimate Aquifer Parameters and Storage Variations of Confined Aquifer System in Cangzhou, North China Plain, Water Resour. Res., 54(10), 8234–8252, doi:10.1029/2017WR022126, 2018.

295 Jousset, P., Reinsch, T., Ryberg, T., Blanck, H., Clarke, A., Aghayev, R., Hersir, G. P., Henninges, J., Weber, M. and Krawczyk, C. M.: Dynamic strain determination using fibre-optic cables allows imaging of seismological and structural features, Nat. Commun., 9(1), 1–11, 2018.

Kinoshita, C. and Saffer, D. M.: In Situ Permeability and Scale Dependence of an Active Accretionary Prism Determined From Cross-Borehole Experiments, Geophys. Res. Lett., 45(14), 6935–6943, doi:10.1029/2018GL078304, 2018.

300 Kishida, K., Yamauchi, Y. and Guzik, A.: Study of optical fibers strain-temperature sensitivities using hybrid Brillouin-Rayleigh System, Photonic Sensors, 4(1), 1–11, 2014.

Kogure, T. and Okuda, Y.: Monitoring the vertical distribution of rainfall-induced strain changes in a landslide measured by distributed fiber optic sensing (DFOS) with Rayleigh backscattering, Geophys. Res. Lett., doi:10.1029/2018GL077607, 2018.

305 Koyamada, Y., Imahama, M., Kubota, K. and Hogari, K.: Fiber-optic distributed strain and temperature sensing with very high measurand resolution over long range using coherent OTDR, J. Light. Technol., 27(9), 1142–1146, 2009.

Krietsch, H., Gischig, V. S., Doetsch, J., Evans, K. F., Villiger, L., Jalali, M., Valley, B., Loew, S. and Amann, F.: Hydro-mechanical processes and their influence on the stimulation effected volume: Observations from a decameter-scale hydraulic stimulation project, Solid Earth Discuss., 2020, 1–43, doi:10.5194/se-2019-204, 2020.

310 Lei, X., Xue, Z. and Hashimoto, T.: Fiber Optic Sensing for Geomechanical Monitoring:(2)-Distributed Strain Measurements at a Pumping Test and Geomechanical Modeling of Deformation of Reservoir Rocks, Appl. Sci., 9(3), 417, 2019.

Lellouch, A., Yuan, S., Spica, Z., Biondi, B. and Ellsworth, W. L.: Seismic Velocity Estimation Using Passive Downhole Distributed Acoustic Sensing Records: Examples From the San Andreas Fault Observatory at Depth, J. Geophys. Res. Solid 315 Earth, 124(7), 6931–6948, doi:10.1029/2019JB017533, 2019.

Lindsey, N. J., Dawe, T. C. and Ajo-franklin, J. B.: Illuminating seafloor faults and ocean dynamics with dark fiber distributed acoustic sensing, , 1107(November), 1103–1107, 2019.

Lindsey, N. J., Rademacher, H. and Ajo-Franklin, J. B.: On the Broadband Instrument Response of Fiber-Optic DAS Arrays, J. Geophys. Res. Solid Earth, 125(2), e2019JB018145, doi:10.1029/2019JB018145, 2020.

320   Luo, H., Li, H., Lu, Y., Li, Y. and Guo, Z.: Inversion of distributed temperature measurements to interpret the flow profile for a multistage fractured horizontal well in low-permeability gas reservoir, Appl. Math. Model., 77, 360–377, doi:https://doi.org/10.1016/j.apm.2019.07.047, 2020.

Maldaner, C. H., Munn, J. D., Coleman, T. I., Molson, J. W. and Parker, B. L.: Groundwater Flow Quantification in Fractured Rock Boreholes Using Active Distributed Temperature Sensing Under Natural Gradient Conditions, Water

325   Resour. Res., 55(4), 3285–3306, doi:10.1029/2018WR024319, 2019.

Mouli-Castillo, J., Wilkinson, M., Mignard, D., McDermott, C., Haszeldine, R. S. and Shipton, Z. K.: Inter-seasonal compressed-air energy storage using saline aquifers, Nat. Energy, 4(2), 131–139, 2019.

Murdoch, L. C., Freeman, C. E., Germanovich, L. N., Thrash, C. and DeWolf, S.: Using in situ vertical displacements to characterize changes in moisture load, Water Resour. Res., 51(8), 5998–6016, doi:10.1002/2015WR017335.Received, 2015.

330   Murdoch, L. C., Germanovich, L. N., DeWolf, S. J., Moysey, S. M. J., Hanna, A. C., Kim, S. and Duncan, R. G.: Feasibility of using in situ deformation to monitor CO_2 storage, Int. J. Greenh. Gas Control, 93(September 2018), 102853, doi:10.1016/j.ijggc.2019.102853, 2020.

Neuzil, C. E.: Hydromechanical coupling in geologic processes, Hydrogeol. J., 11(1), 41–83, 2003.

Rutqvist, J., Rinaldi, A. P., Cappa, F., Jeanne, P., Mazzoldi, A., Urpi, L., Guglielmi, Y. and Vilarrasa, V.: Fault activation

335   and induced seismicity in geological carbon storage – Lessons learned from recent modeling studies, J. Rock Mech. Geotech. Eng., 8(6), 789–804, doi:10.1016/j.jrmge.2016.09.001, 2016.

Schenato, L.: A review of distributed fibre optic sensors for geo-hydrological applications, Appl. Sci., 7(9), doi:10.3390/app7090896, 2017.

Schuite, J., Longuevergne, L., Bour, O., Boudin, F., Durand, S. and Lavenant, N.: Inferring field-scale properties of a

340   fractured aquifer from ground surface deformation during a well test, Geophys. Res. Lett., 42(24), 10–696, 2015.

Schuite, J., Longuevergne, L., Bour, O., Burbey, T. J., Boudin, F., Lavenant, N. and Davy, P.: Understanding the hydromechanical behavior of a fault zone from transient surface tilt and fluid pressure observations at hourly time scales, Water Resour. Res., 53(12), 10558–10582, 2017.

Schweisinger, T., Svenson, E. J. and Murdoch, L. C.: Introduction to hydromechanical well tests in fractured rock aquifers,

345   Ground Water, 47(1), 69–79, doi:10.1111/j.1745-6584.2008.00501.x, 2009.

Shanafield, M., Banks, E. W., Arkwright, J. W. and Hausner, M. B.: Fiber-optic Sensing for Environmental Applications: Where We've Come From- and What's Possible?, Water Resour. Res., 2012–2017, doi:10.1029/2018WR022768, 2018.

Smith, R. and Knight, R.: Modeling Land Subsidence Using InSAR and Airborne Electromagnetic Data, Water Resour. Res., 55(4), 2801–2819, doi:10.1029/2018WR024185, 2019.

350   Sun, Y., Xue, Z., Hashimoto, T. and Lei, X.: Distributed Fiber Optic Sensing System for Well-based Monitoring Water Injection Tests — A Geomechanical Responses Perspective, Water Resour. Res., 56, 1–30, 2020.

des Tombe, B. F., Bakker, M., Smits, F., Schaars, F. and van der Made, K.: Estimation of the variation in specific discharge over large depth using Distributed Temperature Sensing (DTS) measurements of the heat pulse response, Water Resour. Res., 55(1), 811–826, 2019.

355   Vasco, D. W., Ferretti, A. and Novali, F.: Reservoir monitoring and characterization using satellite geodetic data: Interferometric synthetic aperture radar observations from the Krechba field, Algeria, Geophysics, 73(6), WA113-WA122, 2008.

Vasco, D. W., Rucci, A., Ferretti, A., Novali, F., Bissell, R. C., Ringrose, P. S., Mathieson, A. S. and Wright, I. W.: Satellite-based measurements of surface deformation reveal fluid flow associated with the geological storage of carbon dioxide,

360   Geophys. Res. Lett., 37(3), 2010.

Vasco, D. W., Harness, P., Pride, S. and Hoversten, M.: Estimating fluid-induced stress change from observed deformation, Geophys. J. Int., 208(3), 1623–1642, doi:10.1093/gji/ggw472, 2017.

Vilarrasa, V., Carrera, J. and Olivella, S.: Hydromechanical characterization of CO2 injection sites, Int. J. Greenh. Gas Control, 19, 665–677, 2013.

365   Wang, H. F.: Theory of linear poroelasticity with applications to geomechanics and hydrogeology, Princeton University Press., 2017.

Xue, Z., Shi, J.-Q., Yamauchi, Y. and Durucan, S.: Fiber Optic Sensing for Geomechanical Monitoring: (1)-Distributed Strain Measurements of Two Sandstones under Hydrostatic Confining and Pore Pressure Conditions, Appl. Sci., 8(11), 2103, doi:10.3390/app8112103, 2018.

370   Yeh, T. J. and Liu, S.: Hydraulic tomography: Development of a new aquifer test method, Water Resour. Res., 36(8), 2095–2105, 2000.

Zhang, C., Shi, B., Gu, K., Liu, S., Wu, J., Zhang, S., Zhang, L., Jiang, H. and Wei, G.: Vertically distributed sensing of deformation using fiber optic sensing, Geophys. Res. Lett., 45(21), 11–732, 2018.

Zhang, Y. and Xue, Z.: Deformation-Based Monitoring of Water Migration in Rocks Using Distributed Fiber Optic Strain

375   Sensing: A Laboratory Study, Water Resour. Res., 55(11), 8368–8383, 2019.

Zhang, Y., Xue, Z., Park, H., Shi, J., Kiyama, T., Lei, X., Sun, Y. and Liang, Y.: Tracking CO2 Plumes in Clay-Rich Rock by Distributed Fiber Optic Strain Sensing (DFOSS): A Laboratory Demonstration, Water Resour. Res., 55(1), 856–867, 2019.

Zhu, T. and Stensrud, D. J.: Characterizing Thunder-Induced Ground Motions Using Fiber-Optic Distributed Acoustic

380   Sensing Array, J. Geophys. Res. Atmos., 124, 12810– 12823, 2019.

Figure 1: (a) Well pattern for wells obs1 and obs2, in which optical fibers were installed, and the new drilled well; (b) schematic of drilling fluid invading the reservoir formation; and (c) axial cross section of the well showing the area behind the casing installation of optical fiber cable.
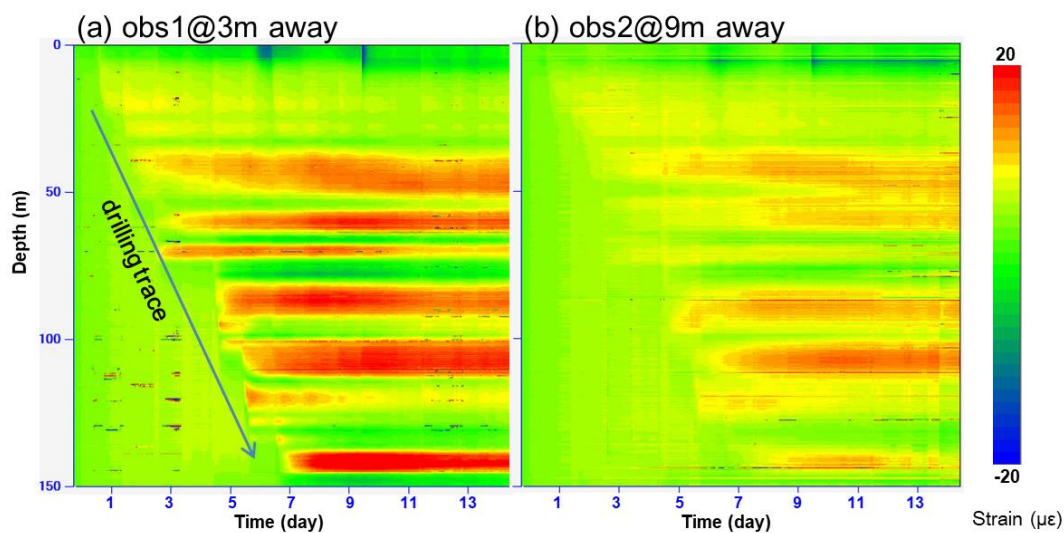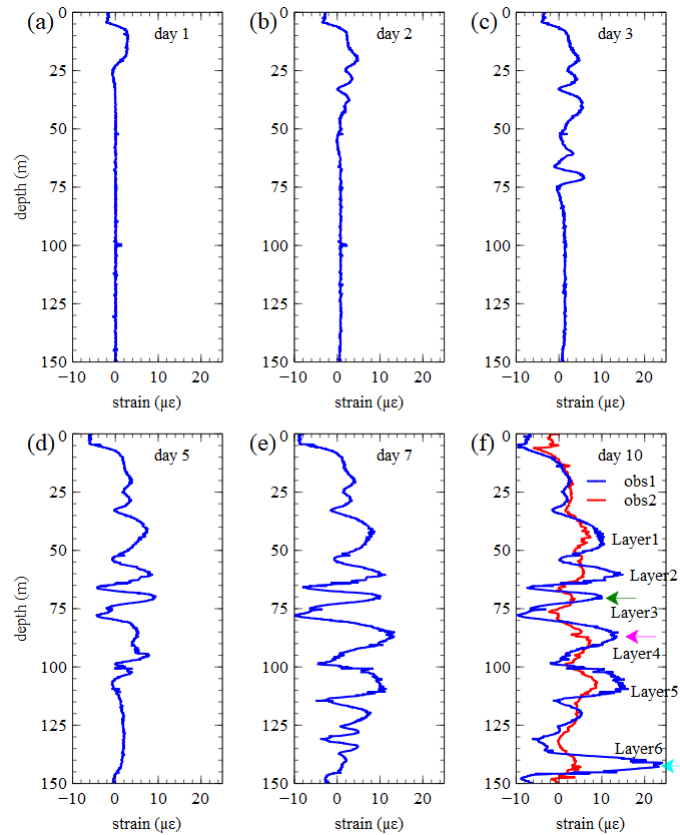
385

Figure 2: Contours of strain changes with time and depth at (a) well obs1 and (b) well obs2.

Figure 3: Strain profiles along obs1 well on different days. The strain profile of obs2 at day 10 is added in (f) for comparison. The time series of the strain changes for the three arrows refer to depths shown in Fig. S3.
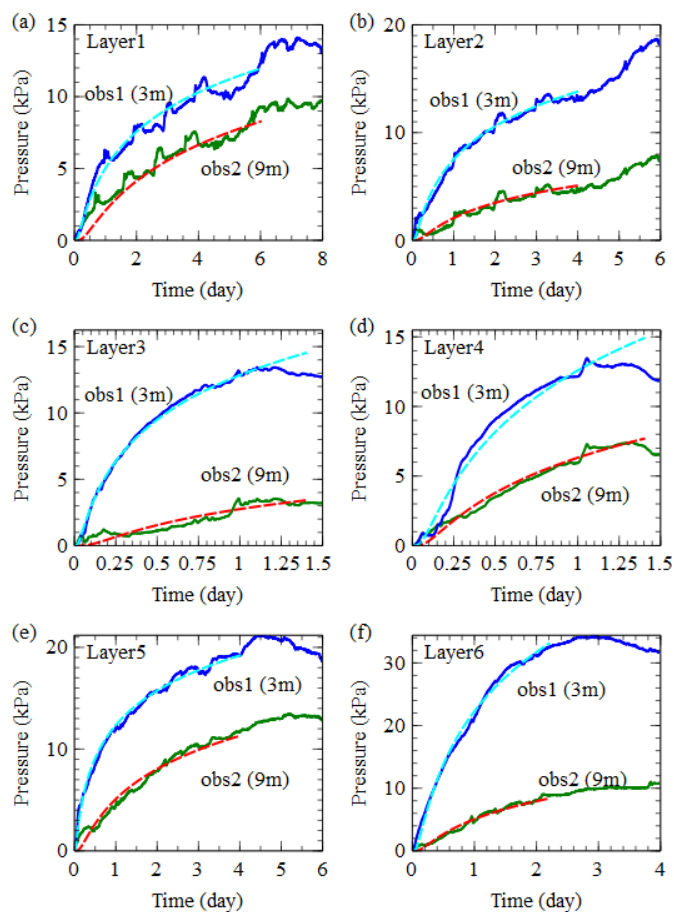
Figure 4: Best matched pressure diffusion models (dashed lines) for six selected layers (1–6; corresponding to a–f) at the sites of obs1 (3 m) and obs2 (9 m).

Table 1. Fitted permeability (m^2) of each layer for interpreting the strain changes.

Layer	1	2	3	4	5	6
obs1 (3m)	7.0E-17	9.6E-16	2.7E-15	1.1E-15	2.6E-15	8.9E-16
obs2 (9m)	3.6E-16	3.8E-16	6.2E-16	7.7E-16	4.9E-16	5.1E-16

395